Letters

A Fast High-Order Solver for EM Scattering from Complex Penetrable Bodies: TE Case

Oscar P. Bruno and Alain Sei

***Abstract*—We present a new high-order integral algorithm for the solution of scattering problems by heterogeneous bodies under TE radiation. Here, a scatterer is represented by a (continuously or discontinuously) varying refractive index $n(x)$ within a two-dimensional (2-D) bounded region; solutions of the associated Helmholtz equation under given incident fields are then obtained by high-order inversion of the Lippmann–Schwinger integral equation. The algorithm runs in $\mathcal{O}(N \log(N))$ operations, where N is the number of discretization points. Our method provides highly accurate solutions in short computing times, even for problems in which the scattering bodies contain complex geometric singularities.**

***Index Terms*—Electromagnetic (EM) scattering, iterative methods, nonhomogenous media.**

I. Introduction

We present a new high-order integral algorithm for the solution of problems of electromagnetic (EM) scattering requiring *two-dimensional* (2-D) integration. We restrict ourselves to the simplest EMs problem in which 2-D singular integrals occur: scattering by a 2-D heterogeneous body under TE polarized radiation. A basic element in our method is the use of truncated Fourier expansions of the Green function of the problem. The logarithmic point-singularities of the Green function manifest themselves, in the finite Fourier approximations, as singular arcs inside the integration domain; see (3). Such singularity distributions allow for computation of the required 2-D integrals by means of simple 1-D *high-order* integrators. The algorithm is fast: it runs in $\mathcal{O}(N \log(N))$ operations, where N is the number of discretization points. It can be applied to general configurations, including scatterers in which the refractive index varies discontinuously. An example is provided of a highly singular scattering configuration containing cusps, for which solutions with errors of order $10^{(-5)}$ are obtained in a 13-s computation on a desktop computer. Thus, the performance of the present algorithm in general cases improves by many orders of magnitude over that exhibited by other methods available at present.

Our approach is related to the well-known k-space method [1], which is based on representation of the solution by its Fourier transform, in cartesian coordinates, in all of space. In this case, truncation of the Fourier transform at wavenumbers K leads to errors of the order of $1/K$, and thus, the error in the k-space method is of order one in the mesh-size (compare analysis and numerical results given in [4]). Our method takes advantage of the highly accurate approximations provided by Fourier series in the periodic case, and it thus achieves the claimed high-order accuracy, see Section IV.

Manuscript received October 5, 1999; revised June 26, 2000. This work was supported by the Air Force Office of Scientific Research, Air Force Materials Command, USAF under Grant F49620-96-1-0008. The work of O. P. Bruno was supported by NSF under Contracts DMS-9523292 and the Air Force Office of Scientific Research, Air Force Materials Command, USAF under Grant F49620-99-1-0010 and F49620-99-1-0193.

O. P. Bruno is with Applied Mathematics, Caltech, Pasadena, CA 91125 USA.

A. Sei is with the Ocean Technology Department, TRW, Redondo Beach, CA 90266 USA.

Publisher Item Identifier S 0018-926X(00)10843-9.

II. Preliminaries

We consider a scattering configuration in which a bounded scatterer Ω is contained within a radius R from the origin; the relevant nondimensional size is given by $\kappa R = 2\pi R/\lambda$. The refractive index $n(x)$ varies arbitrarily in Ω and $n(x) = 1$ outside the scatterer. Thus, setting $m(x) = 1 - n^2(x)$, for $|x| > R$ we have $n(x) = 1$ and $m(x) = 0$. For a given incident field u^{inc}, the total field u, equal to the sum of u^{inc} and the scattered field u^s, is a solution of Helmholtz's equation $\Delta u + \kappa^2 n^2(x) u = 0$ or, alternatively, a solution of the Lippmann–Schwinger integral equation

$$u(x) = u^{inc}(x) - \frac{i\kappa^2}{4} \int_\Omega H_0^1(\kappa|x-y|) m(y) u(y)\, dy \qquad (1)$$

where H_0^1 is the Hankel function of the first kind; see, e.g., [2]. We solve this equation by the iterative technique GMRES [3], which requires repeated evaluations of the right-hand side (RHS) of (1) for given inputs u. The accuracy of the calculation is limited by that of the integral evaluations; thus our focus on high-order singular quadrature rules.

III. Numerical Method

Our algorithm is based on use of the addition theorem, which provides a mean to integrate to high order the singular integrand in (1). We thus use polar coordinates $x = ae^{i\psi}$ and $y = re^{i\theta}$ so that the integral on the RHS of (1) becomes

$$K[u](a,\psi) = -\frac{i\kappa^2}{4} \int_0^R r\,dr \int_0^{2\pi} \cdot H_0^1(\kappa|ae^{i\psi} - re^{i\theta}|) m(r,\theta) u(r,\theta)\, d\theta. \qquad (2)$$

Expanding the kernel in (2) via the addition theorem for the Hankel function

$$H_0^1(\kappa|ae^{i\psi} - re^{i\theta}|) = \sum_{\ell=-\infty}^{+\infty} \mathcal{J}_\ell(a,r) e^{i\ell(\psi-\theta)}$$
$$\mathcal{J}_\ell(a,r) = J_\ell(\kappa \min(a,r)) H_\ell^1(\kappa \max(a,r)) \qquad (3)$$

and introducing the Fourier series expansion $K[u](a,\psi) = \sum_{\ell=-\infty}^{\infty} K_\ell[u](a) e^{i\ell\psi}$ we then obtain the expression

$$K_\ell[u](a) = -\frac{i\kappa^2}{4} \int_0^R \mathcal{J}_\ell(a,r) r\,dr \int_0^{2\pi} m(r,\theta) u(r,\theta) e^{-i\ell\theta}\, d\theta \qquad (4)$$

which is a centerpiece of our algorithm. The discontinuities of m are the only obstacles to high-order integration in θ. To deal with such discontinuities we approximate m by a truncated Fourier series $m^F(a,\psi) = \sum_{\ell=-F}^{F} m_\ell(a) e^{i\ell\psi}$. For finite F, m^F provides a smooth approximation of m and therefore allows for high-order θ integration. (As our numerical results demonstrate, extremely accurate approximations of near fields and far fields can be obtained for relatively small values of F; this fact is what makes our approach

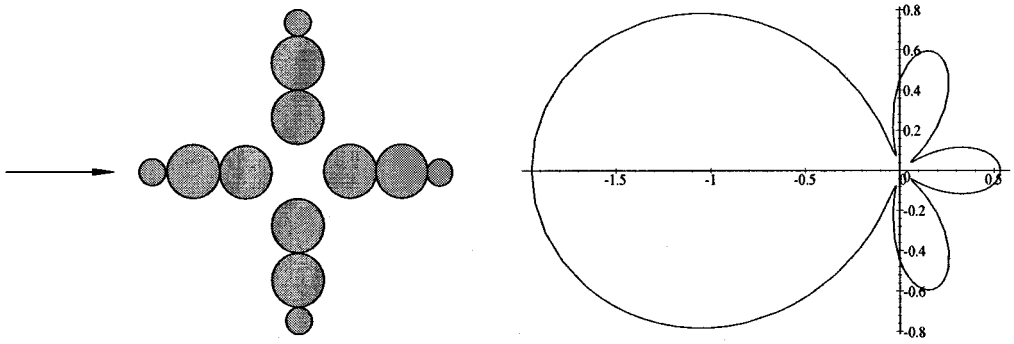

Fig. 1. A scattering configuration and its far-field pattern.

TABLE I
ERRORS AND TIMINGS FOR THE CONFIGURATION OF FIG. 1: $N_p = 3$ AND $\kappa R = 3$ SHOWING A LINEAR DEPENDENCE OF INTEGRATION TIMES AND OVERHEAD $M \cdot N_r$

n^2	M	N_θ	N_r	# Iter	OH(s)	NO(ms)	Tot. Time(s)	NT(ms)	Error (Far Field)
2	10	121	23	2	0.593	2.5	1.934	72	1 (-3)
2	20	131	31	2	1.273	2.0	5.007	75	1 (-4)
2	30	141	43	3	2.332	1.8	12.794	67	3 (-5)
72	10	121	19	2	0.611	3.2	8.678	52	3 (-1)
72	20	141	33	3	1.666	2.5	46.952	57	7 (-2)
72	30	225	63	6	4.110	2.2	264.233	57	7 (-3)

viable.) Analogously, we define $u^M(r) = \sum_{l=-M}^{M} u_\ell(r)e^{i\ell\theta}$, $I_\ell^{F,M}(r) = \int_0^{2\pi} m^F(r,\theta)u^M(r,\theta)e^{-i\ell\theta}\,d\theta$ and

$$K_\ell^{F,M}[u](a) = -\frac{i\kappa^2}{4}\int_0^R \mathcal{J}_\ell(a,r)I_\ell^{F,M}(r)r\,dr. \tag{5}$$

Now we note that the integrand defining $I_\ell^{F,M}(r)$ is a periodic regular function of θ. Thus, the θ integration can be performed by means of the trapezoidal rule, which, in addition to being exponentially accurate, can be evaluated with a reduced operation count by means of the FFT. Our integration problem now reduces to evaluation of radial integrals via high order quadrature. To compute the integral in (5) we note that

$$K_\ell[u](a) = H_\ell^1(\kappa a)\int_0^{\min(a,R)} J_\ell(\kappa r)I_\ell^{F,M}(r)r\,dr + J_\ell(\kappa a)\int_{\min(a,R)}^{R} H_\ell^1(\kappa r)I_\ell^{F,M}(r)r\,dr. \tag{6}$$

We assume $I_\ell^{F,M}(r)$ is differentiable to a sufficiently high order. This is not a restrictive condition since appropriate changes of variables can be used to resolve the singularities that may occur in this function. The radial integration algorithm we have devised is based on polynomial interpolations. To evaluate $K_\ell[u]$ we divide the radial integration domain in a number N_i of interpolation intervals. Within each interval $u_\ell(r)$ is interpolated by a polynomial of degree $N_p - 1$, thus yielding errors of order h^{N_p} for a mesh size of order h. For adequate values of N_p direct integration of these polynomials provides accurate approximations of $K_\ell[u]$. The overall complexity of the method is $N\log(N)$, where calling $N_r = N_i(N_p - 1) + 1$ the number of points in the discretizations for the r variable, $N = N_r M$. (Note that the angular discretization parameter N_θ does not appear explicitly in this complexity estimate: the number M of Fourier modes is used instead.)

IV. NUMERICAL RESULTS

We have produced solutions for a large class of scattering configurations, including smooth scatterers as well as scatterers with singularities such as corners and cusps. In the case of a circular cylinder where analytical solutions are available, double-precision accuracies were obtained in short computing times. A nontrivial comparison with an exact solution as discussed below is also presented, showing convergence consistent with that obtained in the more complex cases. In what follows we present calculations for one of the most challenging geometric configurations we have treated, containing discontinuities and cusps in the distribution of refractive index, see Fig. 1. We first show results for low values of the refractive index, $n^2 = 2$, and then, following [4], for the much larger value $n^2 = 72$. In fact there is no limit to the complexity of the problem that can be treated provided appropriate discretizations are utilized; see Table I. All the reported computations were performed on a single-processor 200-MHz Silicon Graphics R-10000 desktop computer.

We thus consider the scattering configuration depicted in Fig. 1, formed by 12 touching circles of refractive index n, 8 of radius 0.5, and 4 of radius 0.25, in such a way that the smallest circle containing the scatterer has radius $R = 3$. The cusps in this geometry are well known to present severe difficulties to other algorithms. For such a dis-

continuous refractive index it is necessary to use Fourier smoothing; the value $F = 100$ was used here. (Thorough numerical tests, including comparison with the exact solution mentioned below as well as convergence tests, have shown that the values of the smoothing parameter F we used give converged solutions within the error bars quoted.) Table I shows convergence studies for $n^2 = 2$ and $n^2 = 72$. Errors in the table (maximum absolute values in the far field) were obtained by comparison with a much more refined discretization: $F = 200$, $M = 100$, $N_r = 181$, and $N_\theta = 301$ in the case $n^2 = 2$, and $F = 200$, $M = 40$, $N_r = 301$, and $N_\theta = 295$ for $n^2 = 72$. Near field errors are generally larger by a factor of 10. As claimed, our algorithm resolves the $n^2 = 2$ configuration with an error of order $10^{(-5)}$ in a 13-s run. The restart parameter required by GMRES was taken to equal 4 in the case $n^2 = 2$ and to equal 40 for $n^2 = 72$. OH denotes the overhead, and NO and NT denote the normalized quantities $\text{NO} = 10^3\text{OH}/(M \cdot N_r)$ $\text{NT} = 10^3(\text{Time} - \text{OH})/(\text{Restart} \cdot \text{Iter} \cdot M \cdot N_r)$. In order to insure that these tests give an accurate measure of the error we applied the same procedure to an off-center circle for which an analytical solution is known. This geometry provides a nontrivial test for our solver since it involves discontinuities in the refractive index within the domain of integration. Our test circle has radius one and is centered at (2, 0). For $n^2 = 2$ using $M = 10$, 20, and 40 our solver yields errors of $2(-4)$, $3(-5)$, and $4(-6)$, respectively. For $n^2 = 72$ using $M = 10$, 20, and 40 modes we obtained errors of $3(0)$, $2(-2)$, and $2(-3)$, respectively, in good agreement with the orders of the errors shown in Table I.

REFERENCES

[1] N. N. Bojarski, "The k-space formulation of the scattering problem in the time domain," *J. Opt. Soc. Amer.*, vol. 72, pp. 570–584, 1982.

[2] D. Colton and R. Kress, *Inverse Acoustic and Electromagnetic Scattering Theory*. New York: Springer-Verlag, 1992.

[3] Y. Saad and M. H. Schultz, "GMRES: A generalized minimal residual algorithm for solving non-symmetric linear systems," *SIAM J. Sci. Statist. Comput.*, vol. 7, pp. 856–869, 1986.

[4] P. Zwamborn and P. Van den Berg, "Three dimensional weak form of the conjugate gradient FFT method for solving scattering problems," *IEEE Trans. Microwave Theory Tech.*, vol. 40, pp. 1757–1766, Sept. 1992.

A Low-Profile Conical Beam Loop Antenna with an Electromagnetically Coupled Feed System

H. Nakano, K. Fujimori, and J. Yamauchi

***Abstract*—The radiation characteristics of a low-profile loop antenna are evaluated using the method of moments (MoM). The loop having a circumference of approximately two wavelengths is electromagnetically coupled to a bent feed line and radiates a circularly polarized conical beam. The frequency bandwidth for a 3-dB axial ratio criterion is calculated to be approximately 0.5% for an antenna height of $h = 0.064$ wavelengths. Over the same bandwidth, the input impedance is approximately 50 ohms and the gain is approximately 7 dB.**

***Index Terms*—Electromagnetically coupled feed, loop.**

I. INTRODUCTION

It is well known that a loop antenna is a linearly polarized (LP) radiation element [1], [2]. Recent theoretical study has revealed that, when two perturbation elements are added to a one-wavelength circumference loop [3], an LP axial beam can be changed to a circularly polarized (CP) axial beam.

Automobile communication systems often require a CP conical beam antenna in addition to a CP axial beam antenna. For this requirement, this letter presents a low-profile loop antenna that radiates a CP conical beam. For CP conical beam formation, a single perturbation element is added to a loop whose circumference is approximately two wavelengths.

Attention is paid to input impedance matching. To reduce the high-input impedance of the conventional loop antenna fed directly from a coaxial line, an electromagnetically coupled feed system is proposed. The feed line in this system is not in contact with the loop, leading to straightforward impedance matching.

II. DISCUSSIONS

Fig. 1 shows the configuration and coordinate system of a low-profile loop antenna. The loop is made of a thin wire of radius ρ. The loop of circumference C, backed by a conducting ground plane, has a perturbation element of length ΔL at point b. The distance from the ground plane to the loop section (antenna height) and the angle made by the x axis with line o'-b (perturbation angle) are designated as h and ϕ_b, respectively. The loop is supported by a dielectric material of relative permittivity ε_r.

The feed system consists of a bent wire f-c-d of radius ρ_F, which is electromagnetically coupled to the loop (EM-coupled feed). The curved section of the feed wire c-d is parallel to the loop and located just under the loop. The vertical section f-c and the parallel section c-d have lengths of L_V and L_H, respectively.

Throughout this letter, the following parameters are chosen to be as follows: $\rho = 0.003\lambda_0 = 0.6$ mm, $h = 0.064\lambda_0 = 12.8$ mm, $\varepsilon_r \approx 1$ (honeycomb material is used for a spacer), and $\rho_F = 0.0031\lambda_0 = 0.62$ mm, where λ_0 (=200 mm) is the wavelength at a design frequency of $f_0 = 1.5$ GHz.

The loop circumference, perturbation element length, and bent wire length are initially chosen to be $C = 2\lambda_0$, $\Delta L = 0.025$ C, and $L_V + L_H = \lambda_0/4$, respectively. Then these values are optimized such that

Manuscript received March 14, 1997; revised July 10, 2000.

The authors are with the College of Engineering, Hosei University, Koganei, Tokyo 184-8584 Japan (e-mail: nakano@k.hosei.ac.jp).

Publisher Item Identifier S 0018-926X(00)10838-5.

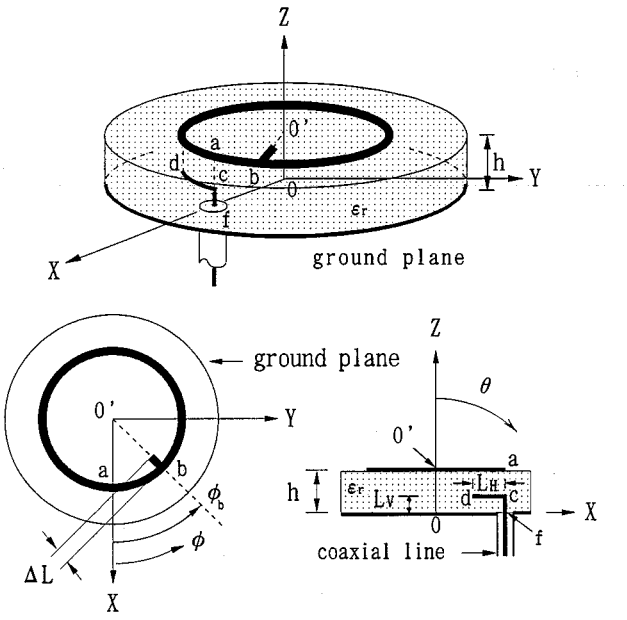

Fig. 1. Configuration and coordinate system.

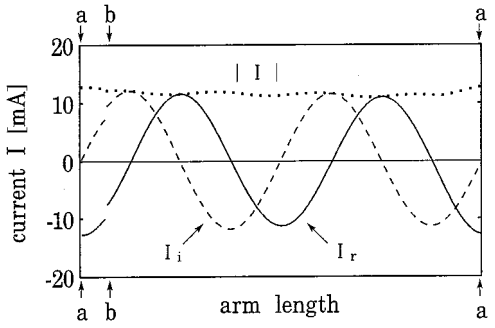

Fig. 2. Current distribution.

the antenna radiates a circularly polarized wave with an antenna input impedance of 50 ohms at the design frequency f_0, resulting in $C = 1.986\lambda_0$, $\Delta L = 0.05\lambda_0$, and $(L_V, L_H) = (0.023\lambda_0, 0.226\lambda_0)$. For confirmation of the analysis, experimental results are obtained for $f_0 = 1.5$ GHz, using these configuration parameters.

The method of moments (MoM) is used to obtain the current distribution. The theoretical radiation pattern, axial ratio, gain, and input impedance are evaluated on the basis of the obtained current distribution. Note that the ground plane in Fig. 1 is assumed to be of infinite extent.

Fig. 2 shows the theoretical current distribution at frequency f_0, where the perturbation angle ϕ_b is chosen to be $90^\circ/4 = 22.5^\circ$. A traveling-wave current flows along the loop section. The amplitude of the current $|I|$ $(I = I_r + jI_i)$ is almost constant. The discontinuity of the current at point b is due to the perturbation element. Note that Kirchihoff's current law is satisfied at branch point b.

The traveling current yields CP radiation. A right-hand CP wave is obtained with $\phi_b = 90^\circ/4 + 90^\circ n$ $(n = 0, 1, 2, 3)$, and a left-hand CP wave is obtained with $\phi_b = 90^\circ(3/4) + 90^\circ n$ $(n = 0, 1, 2, 3)$. The rotational sense alternates with an angle period of 45°. In the following discussion, the perturbation angle ϕ_b is fixed to be $\phi_b = 90^\circ/4$.

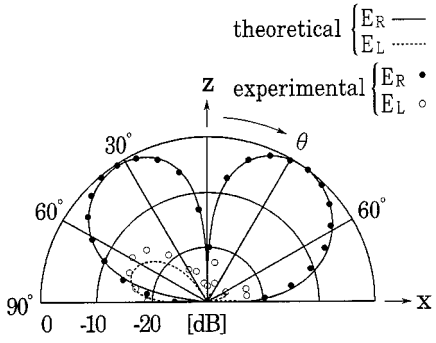

Fig. 3. Radiation pattern in the $\phi = 0^\circ$ plane.

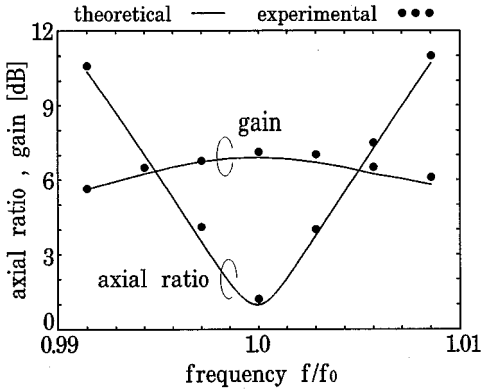

Fig. 4. Axial ratio and gain as a function of frequency.

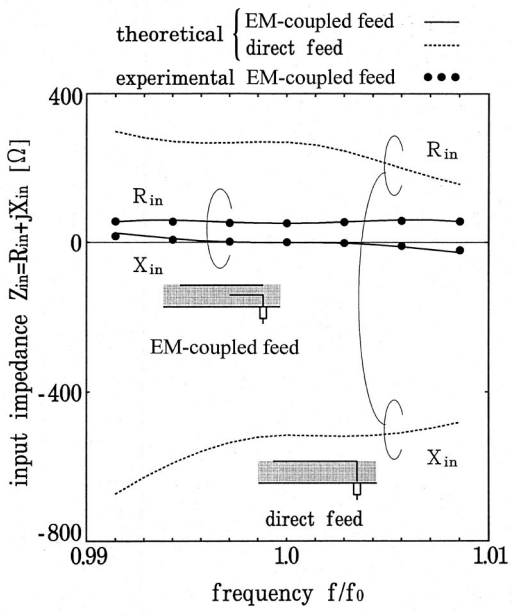

Fig. 5. Input impedance as a function of frequency.

Fig. 3 shows the theoretical radiation pattern at f_0 in the $\phi = 0^\circ$ plane, where E_R (solid line) and E_L (dashed line) are the intensities of the right- and left-hand CP waves, respectively. The copolar component (E_R) has a maximum value in the $\theta = 34^\circ$ direction and the variation in E_R at $\theta = 34^\circ$ as a function of azimuth angle ϕ is very small (less

than 1.1 dB). That is, a CP conical beam is formed. Note that the cross-polarization component (E_L) at $\theta = 34^\circ$ as a function of azimuth angle ϕ is very small, leading to good axial ratios of less than 2.2 dB.

The frequency response for the axial ratio in the direction $(\theta, \phi) = (34^\circ, 0^\circ)$ is shown in Fig. 4, together with the gain. The frequency bandwidth for a 3-dB axial ratio criterion is calculated to be approximately 0.5%. The gain within the same bandwidth is almost constant (approximately 7 dB).

The behavior of the input impedance, $Z_{\rm in} = R_{\rm in} + jX_{\rm in}$, as a function of frequency is shown in Fig. 5. For comparison, the input impedance when the loop is directly fed from a coaxial line (designated as the direct feed), as shown in the inset in Fig. 5, is also presented. It is found that the high-input impedance for the direct feed is reduced to 50 ohms using the EM-coupled feed, by which the antenna is easily matched to a commercially available coaxial line.

III. Conclusion

A low-profile loop antenna (antenna height $h = 0.064\lambda_0$), whose circumference is approximately two wavelengths, has been analyzed using the MoM. This loop has a single perturbation element. It is found that the loop radiates a circularly polarized conical beam with a gain of approximately 7 dB over a frequency bandwidth of approximately 0.5%. It is also found that the EM-coupled feed leads to an input impedance of 50 ohms.

Acknowledgment

The authors would like to thank V. Shkawrytko for his assistance in the preparation of this manuscript.

References

[1] R. C. Johnson, *Antenna Engineering Handbook*, 3rd ed. New York: McGraw-Hill, 1993, ch. 5.

[2] H. Nakano, S. R. Kerner, and N. G. Alexopoulos, "The moment method solution for printed wire antennas of arbitrary configuration," *IEEE Trans. Antennas Propagat.*, vol. 36, pp. 1667–1674, 1988.

[3] H. Nakano, "A numerical approach to line antennas printed on dielectric materials," *Computer Physics Commun.*, vol. 68, pp. 441–450, 1991.

A Coupled Surface-Volume Integral Equation Approach for the Calculation of Electromagnetic Scattering from Composite Metallic and Material Targets

C. C. Lu and W. C. Chew

***Abstract*—A coupled surface-volume integral equation approach is presented for the calculation of electromagnetic scattering from conducting objects coated with materials. Free-space Green's function is used in the formulation of both integral equations. In the method of moments (MoM) solution to the integral equations, the target is discretized using triangular patches for conducting surfaces and tetrahedral cells for dielectric volume. General roof-top basis functions are used to expand the surface and volume currents, respectively. This approach is applicable to inhomogeneous material coating, and, because of the use of free-space Green's function, it can be easily accelerated using fast solvers such as the multilevel fast multipole algorithm.**

I. Introduction

Recently, advance in fast algorithms for computational electromagnetics demonstrated great potential to solve scattering problems with realistic targets. However, significant reduction of computational complexity has been achieved for scattering problems with conducting targets only. To expand the capability of fast solvers to include material or material coated targets, it is necessary to investigate solvers that can model material-coated targets. This is the motivation for the coupled integral-equation approach presented in this letter. It should be pointed out that scattering calculation for composite conducting and dielectric objects has been studied previously [1]–[4] using coupled surface-integral equations and coupled surface- and volume-integral equations [5]. However, [5] used pulse-basis functions and applies to rectangular shaped objects. In this letter, we present a similar formulation but with general roof-top basis function expansion and the tetrahedron discretization of the dielectrics. Hence, the approach from this letter applicable to arbitrarily shaped objects. In the following formulation, the time factor is $\exp\{-i\omega t\}$ and is suppressed.

II. Formulations

The problem is to calculate electromagnetic scattering from material-coated objects. The incident wave induces surface current $\overline{J}_S$ on the conducting surface S of the objects, and also induces volume current $\overline{J}_V$ in the dielectric region V. The total scattered field is the superposition of radiations from the surface current and volume current. Let the radiation from $\overline{J}_S$ and $\overline{J}_V$ be $\overline{E}_S^{sca}$ and $\overline{E}_V^{sca}$, respectively, then

$$\overline{E}_\alpha^{sca} = i\omega\mu_b \int_\alpha \overline{\overline{G}}(\overline{r}, \overline{r}') \cdot \overline{J}_\alpha d\overline{r}', \qquad \alpha = S \text{ or } V \tag{1}$$

where $\overline{\overline{G}} = (\overline{\overline{I}} + \nabla\nabla/k_b^2)\exp\{ik_b|\overline{r} - \overline{r}'|\}/4\pi|\overline{r} - \overline{r}'|$ is the 3-D dyadic Green's function, and k_b is the wavenumber for the background media. The surface integral equation is formed based on the boundary

Manuscript received October 26, 1999; revised June 2, 2000. This work was supported in part by the Office of Naval Research under Award N00014-00-1-0605, and by the Air Force Office of Scientific Research under Grant F49620-96-1-0025.

C. C. Lu is with the Department of Electrical Engineering, University of Kentucky, Lexington, KY 40506 USA.

W. C. Chew is with the Department of Electrical and Computer Engineering, University of Illinois, Urbana-Champaign, Urbana, IL 61801 USA.

Publisher Item Identifier S 0018-926X(00)10841-5.

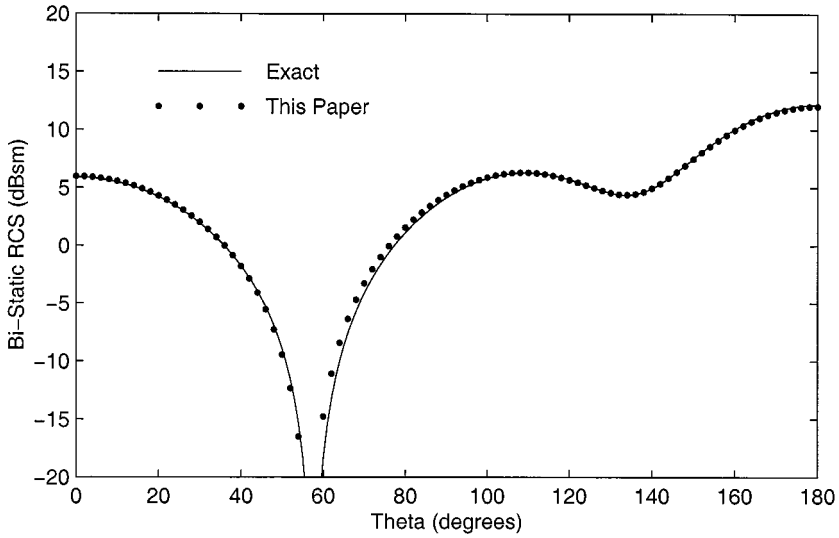

Fig. 1. The calculated RCS of a conducting sphere coated with dielectric material.

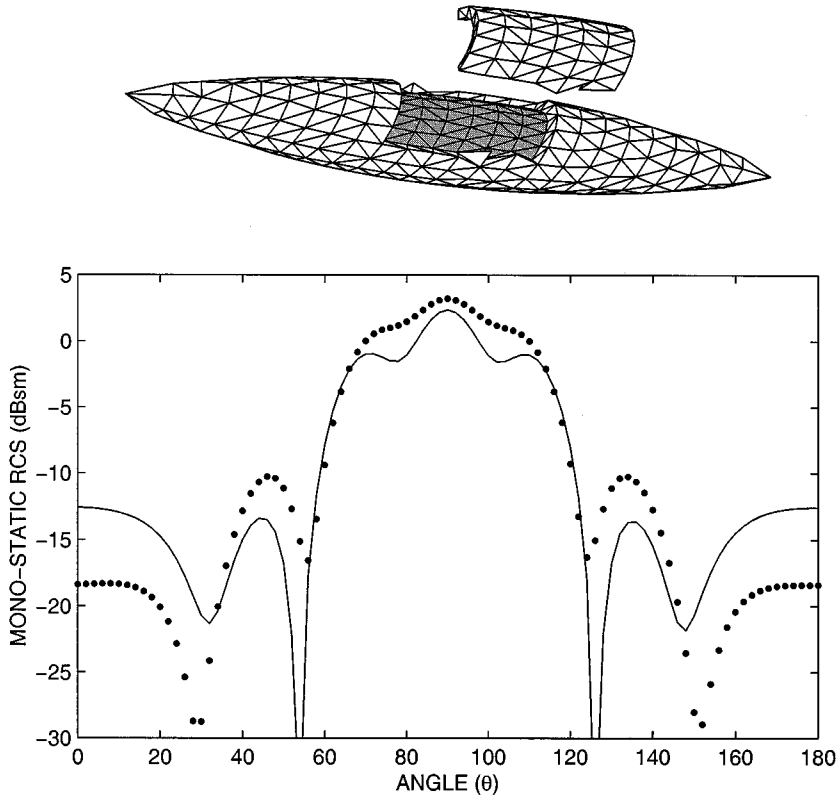

Fig. 2. The calculated RCS of a coated conducting ogive-like object (solid line), and that of a conducting object (dotted line) whose surface is exactly the same as the outermost surface of the coated object. The upper part of the figure shows the geometry mesh.

condition, which requires vanishing tangential component of total electric field

$$\overline{E}_S^{sca}(\overline{r}) + \overline{E}_V^{sca}(\overline{r}) + \overline{E}^i(\overline{r}) = 0, \qquad \overline{r} \in S. \tag{2}$$

The volume-integral equation is formed by writing the total electric field $\overline{E}$ in dielectric as the summation of the incident field $\overline{E}^i$ and the scattered field, i.e.,

$$\overline{E}(\overline{r}) = \overline{E}_S^{sca}(\overline{r}) + \overline{E}_V^{sca}(\overline{r}) + \overline{E}^i(\overline{r}). \tag{3}$$

Since the polarization current is related to the total electric field by $\overline{J}_V = i\omega(\varepsilon_b - \varepsilon)\overline{E}$, we actually have two unknown functions $\overline{J}_S$ and $\overline{J}_V$ in (2) and (3). In the implementation of this letter, $\overline{D} = \varepsilon\overline{E}$ is used as the distribution function in the dielectric.

The coupled-integral equations are converted into matrix equations using the method of moments (MoM) [9]. The procedure consists of subdividing the solution domain into small cells, and representing the induced currents by basis functions that are defined on those small cells. In this letter, small triangular patches are used to model the conducting surface, and the tetrahedron is applied to represent the dielectric region. An arbitrarily shaped object can be accurately

modeled when the cell sizes are small enough. In order to simplify the treatment of conductor-dielectric interface, it is required that the triangular patches coincide with the external faces of tetrahedrons. The surface and volume distribution functions are expanded in terms of 3-D vector basis function that was originally introduced by Rao, Wilton, and Glisson (RWG) in [7] and has also been applied for solving volume-integral equations in [10].

The above selection of volume basis function has an advantage that the normal component of $\overline{D}$ is continuous across the faces between cells. This is consistent with the boundary condition for dielectric interfaces. However, since $\overline{D}$ on the exterior boundary is not necessarily zero, additional degrees of freedom must be introduced to determine $\overline{D}$ on the exterior boundary that interfaces with the background media. This is realized by assigning a "half" basis function for each exterior face of the tetrahedral cell. Hence, a "half" basis function is associated with only one tetrahedron. However, if an exterior face of a tetrahedron is terminated by a conducting patch, then this "half" basis can be removed by using the continuity condition. It can be shown that $\hat{n} \cdot \overline{D} = \nabla \cdot \overline{J}_S / i\omega$, and the coefficients associated to those "half" basis functions are related to a set (M_S) of surface basis coefficients by

$$a_n^V = \sum_{m \in M_S} a_m^S \nabla \cdot \overline{f}_m^S(\bar{r}) \Big/ \left(i\omega \hat{n} \cdot \overline{f}_n^V \right). \tag{4}$$

It should be pointed out that since $\overline{f}_n^V$ is the RWG basis function defined over tetrahedrons, $\hat{n} \cdot \overline{f}_n^V$ is a constant over the tetrahedron surface. Otherwise a testing procedure is needed to determine a_n^V.

III. Numerical Results

In this section two numerical results will be shown. The first result, shown in Fig. 1, is the calculated radar cross section (RCS) of a conducting sphere coated with dielectric material. The radius of the sphere is $0.333\lambda_0$ with $\lambda_0 = 1.5$ m, the coating thickness is $0.0667\lambda_0$, and the dielectric permittivity of the coating material is $\varepsilon_r = 4$. The incident angles are $\theta^i = 0$, $\phi^i = 0$, and the observation angles are $\theta^s = 0$ to 180°, and $\phi^s = 0$. The number of triangular cells used to approximate the conducting surface is 432, and the number of tetrahedral cells to model the coating spherical shell is 1296. The exact solution using Mie series is also shown in the figure as reference.

The second example, shown in Fig. 2, is the calculated radar cross section of a coated ogive-like object. The incident plane wave is in V-pol [i.e., $E_\theta^i = 1$ (V/m) and $E_\phi^i = 0$ for the incident wave at the origin]. The conducting part of this object is formed by joining the bases of two cones. The cones are of the same size and shape with base radius $0.24\lambda_0$ at frequency 300 MHz, and height of $1.0\lambda_0$. The cones are formed by rotating a parabola profile around the z axis. Material with $\varepsilon_r = 2.56 + i0.5$ is uniformly coated over the conducting surface and the coating thickness is $0.07\lambda_0$. Also, shown in Fig. 2 (dotted line) is the RCS of a conducting object whose surface is exactly the same as that of the outermost surface of the coated object. This comparison is to show the effect of material coating. It can be observed that the RCS for the coated object is smaller in the angle range from $\theta^s = 40^\circ$ to $\theta^s = 140^\circ$. However, in the angle range of $(0, 40^\circ)$ and $(140^\circ, 180^\circ)$ the coated object has larger RCS than the conducting object. In other words, for this specific shape, when the incidence angle is close to the normal direction with respect to the surface, the coating has the effect of reducing the RCS. And if the incidence angle is larger (close to grazing incidence), the coating has an opposite effect, the overall RCS is increased. This can be attributed to the excitation of surface waves.

IV. Summary

The coupled surface-volume integral equation for electromagnetic scattering from material coated object is solved using the method of moments. The composite metallic and dielectric object is modeled with mixed triangular surface patch and the tetrahedral volume mesh. Accurate result has been obtained for a coated sphere. The approach presented in this paper is suitable for modeling inhomogeneous material or material coatings. It has the same versatility as the finite-element method in modeling material coating. Therefore, it can be an important alternative to the finite-element method. For instance, when the contrast of the dielectric material is low, this method is a perturbation of the free-space metallic scatterer problem, where rapid convergence by iterative solution is expected. Another important feature of this approach is that both the surface integral equation and the volume integral equation are formulated using the free-space Green's function. This feature makes it easy to apply the multilevel fast multipole solvers to reduce the computational complexity.

References

[1] T. Vaupel and V. Hansen, "Electrodynamic analysis of combined microstrip and coplanar/slotline structure with 3-D components based on a surface/volume integral equation approach," *IEEE Trans. Microwave Theory Tech.*, vol. 47, pp. 1788–1800, Sept. 1999.

[2] B. M. Kolundzuja, "Electromagnetic modeling of composite metallic and dielectric structures," *IEEE Trans. Microwave Theory Tech.*, vol. 47, pp. 1021–1032, July 1999.

[3] S. M. Rao, C. C. Cha, R. L. Cravey, and D. L. Wilkes, "Electromagnetic scattering from arbitrary shaped conducting bodies coated with lossy materials of arbitrary thickness," *IEEE Trans. Antennas Propagat.*, vol. 39, pp. 627–631, May 1991.

[4] L. N. Medgyesi-Mitschang, J. M. Putnam, and M. B. Gedera, "Generalized method of moments for three-dimensional penetrable scatterers," *J. Opt. Soc. Amer. A*, vol. 11, pp. 1383–1398, Apr. 1994.

[5] T. K. Sarkar, S. M. Rao, and A. R. Djordjevic, "Electromagnetic scattering and radiation form finite microstrip structures," *IEEE Trans. Microwave Theory Tech.*, vol. 38, pp. 1568–1575, Nov. 1990.

[6] D. E. Livesay and K. M. Chen, "Electromagnetic fields induced inside arbitrary shaped biological bodies," *IEEE Trans. Microwave Theory Tech.*, vol. 22, pp. 1273–1280, Dec. 1974.

[7] D. H. Schaubert, D. R. Wilton, and A. W. Glisson, "A tetrahedral modeling method for electro-magnetic scattering by arbitrary shaped inhomogeneous dielectric bodies," *IEEE Trans. Antennas Propagat.*, vol. 32, pp. 77–85, Jan. 1984.

[8] R. D. Graglia, "The use of parametric elements in the moment method solution of static and dynamic volume integral equations," *IEEE Trans. Antennas Propagat.*, vol. 36, pp. 636–646, May 1996.

[9] R. F. Harrington, *Field Computation by Moment Methods*. New York: MacMillan, 1968.

[10] S. M. Rao, D. R. Wilton, and A. W. Glisson, "Electromagnetic scattering by surfaces of arbitrary shape," *IEEE Trans. Antennas Propagat.*, vol. 30, pp. 409–418, May 1982.

Single-Feed Circularly Polarized Equilateral-Triangular Microstrip Antenna with a Tuning Stub

Jui-Han Lu and Kin-Lu Wong

***Abstract*—Novel circular polarization (CP) designs of single-feed equilateral-triangular microstrip antennas are proposed and experimentally studied. The proposed CP designs can easily be achieved by loading a narrow tuning stub at the triangle tip or at the center of the bottom edge of the triangular patch. Moreover, by embedding a cross-slot of equal slot lengths in the triangular patch, a compact CP operation can easily be obtained, with an antenna size reduction up to about 22%, as compared to the CP design of a regular triangular microstrip antenna without cross-slot at a fixed frequency.**

***Index Terms*—Circularly polarized radiation, microstrip antenna.**

I. Introduction

It is noted that conventional single-feed circular polarization (CP) designs of microstrip antennas that are available in the open literature are mostly on microstrip antennas with square or circular patches. However, owing to the advantage of having smaller patch size at a given frequency, as compared to square and circular microstrip antennas, some related designs with a triangular microstrip antenna have recently been demonstrated [1]–[4]. In this letter, we demonstrate another promising simple CP design of single-feed triangular microstrip antennas for easy implementation and fine tuning. By simply loading a tuning stub of proper length [5] at the triangular tip or at the center of the bottom edge of the triangular patch [see Fig. 1(a) and (b)], two orthogonal near-degenerate resonant modes can easily be excited for CP operation. Since the tuning stub is of narrow width and is not embedded in the triangular patch as the cases with a slit or a horizontal slot [2], [3], it will be relatively easier to adjust the tuning-stub length to compensate the possible fabrication errors and substrate materials tolerances.

Moreover, by applying the present design with a tuning stub to a compact triangular microstrip antenna with a cross-slot of equal slot lengths (see Fig. 2), CP radiation is also expected to be more easily achieved than the compact CP designs in [3], [6], and [7]. This is because the excitation of two orthogonal near-degenerate modes for CP radiation is now controlled by the tuning stub, not by the small length differences or the slight asymmetry required in the cross-slot [3], the spur lines [6], or the Y-shaped slot [7]. The proposed designs are studied experimentally in this letter.

II. Antenna Configurations

Two configurations of the proposed CP design are depicted in Fig. 1. The triangular patch has a side length of d and is printed on a substrate of thickness h and relative permittivity ε_r. A narrow tuning stub of length ℓ_S and width w is loaded at the triangle tip [Fig. 1(a)] or at the center of the bottom edge of the triangular patch [Fig. 1(b)]. Due to the tuning-stub perturbation, the fundamental mode TM_{10} can be split into two orthogonal near-degenarate modes for CP operation. L_1 and L_2 represent, respectively, the 50-Ω feed-location loci of the two orthogonal modes, which are determined experimentally in this study. By selecting the probe feed at point A, the intersection of loci L_1 and L_2, right-hand CP radiation can be obtained. Left-hand CP radiation is obtained by feeding the patch at point B (the mirror image of point A with respect to the patch's center line).

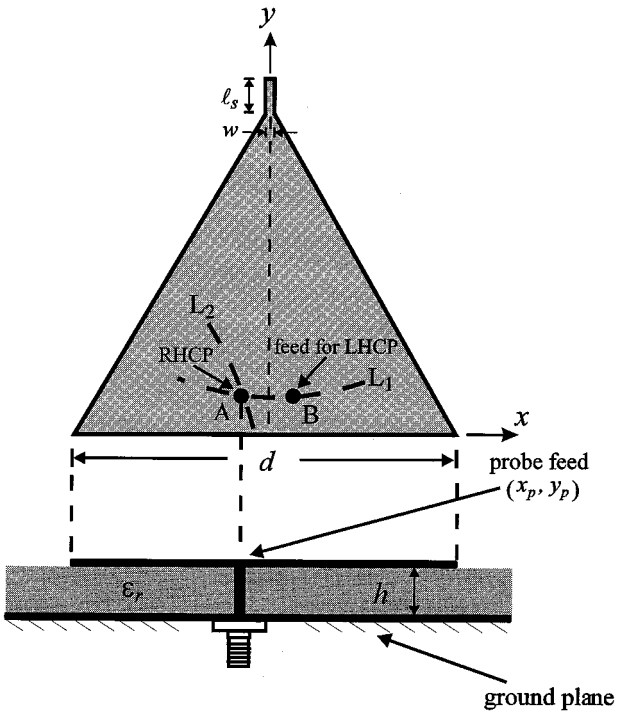

(a)

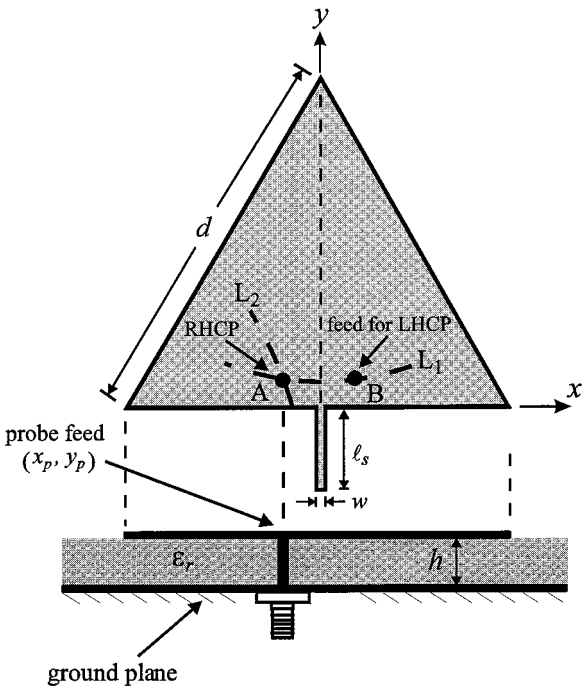

(b)

Fig. 1. Configurations of a single-feed equilateral-triangular microstrip antenna with a tuning stub placed at (a) the triangle tip and (b) the bottom edge of the triangular patch for CP radiation.

Manuscript received May 10, 1999; revised June 7, 2000. This work was supported by the National Science Council of the Republic of China under Grant NSC 89-2213-E-022-001 and Grant NSC 89-2213-E-022-003.

J.-H. Lu is with the Department of Electronic Communication Engineering, National Kaohsiung Institute of Marine Technology, Kaohsiung, Taiwan.

K.-L. Wong is with the Department of Electrical Engineering, National Sun Yat-Sen University, Kaohsiung, Taiwan.

Publisher Item Identifier S 0018-926X(00)10842-7.

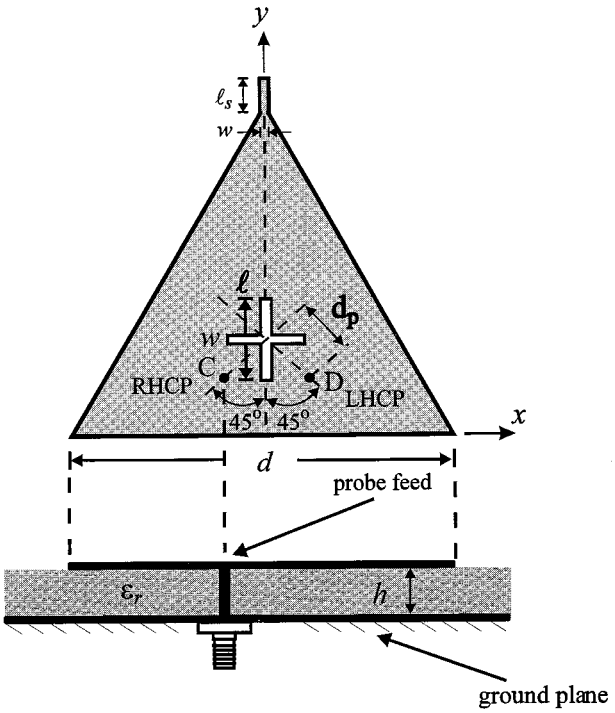

Fig. 2. Configuration of a single-feed compact equilateral-triangular microstrip antenna with a cross-slot of equal slot lengths for CP radiation.

TABLE I
CP PERFORMANCE OF THE PROPOSED ANTENNA SHOWN IN FIG. 1(a); $\varepsilon_r = 4.4$, $h = 1.6$ mm, $w = 1$ mm, FEED AT POINT A. (a) ANTENNA 1: $\ell_S = 5.6$ mm, $d = 60$ mm, $(x_p, y_p) = (-8.0$ mm, 4.5 mm). (b) ANTENNA 2: $\ell_S = 4.4$ mm, $d = 48$ mm, $(x_p, y_p) = (-5.2$ mm, 5.5 mm). (c) ANTENNA 3: $\ell_S = 3.5$ mm, $d = 40$ mm, $(x_p, y_p) = (-3.5$ mm, 4.0 mm)

	d (mm)	ℓ_S (mm)	Center frequency	CP (3-dB axial-ratio) bandwidth	Max. received power
Antenna 1	60	5.6	1564 MHz	1.15%	-48.72 dBm
Antenna 2	48	4.4	1937 MHz	1.14%	-49.06 dBm
Antenna 3	40	3.5	2325 MHz	1.16%	-49.51 dBm

TABLE II
CP PERFORMANCE OF THE PROPOSED ANTENNA SHOWN IN FIG. 1(b); $\varepsilon_r = 4.4$, $h = 1.6$ mm, $w = 1$ mm, FEED AT POINT A. (a) ANTENNA 4: $\ell_S = 18.1$ mm, $d = 60$ mm, $(x_p, y_p) = (-7.7$ mm, 4.7 mm). (b) ANTENNA 5: $\ell_S = 14.7$ mm, $d = 48$ mm, $(x_p, y_p) = (-5.6$ mm, 3.8 mm). (c) ANTENNA 6: $\ell_S = 12.2$ mm, $d = 40$ mm, $(x_p, y_p) = (-4.5$ mm, 3.2 mm)

	d (mm)	ℓ_S (mm)	Center frequency	CP bandwidth	Maximum received power
Antenna 4	60	18.5	1559 MHz	1.14%	-49.16 dBm
Antenna 5	48	14.7	1925 MHz	1.09%	-49.45 dBm
Antenna 6	40	12.2	2300 MHz	1.13%	-49.87 dBm

The proposed CP design for a compact equilateral-triangular microstrip antenna is shown in Fig. 2. The case with the tuning stub placed at the triangle tip is considered. The cross-slot has a length of ℓ and the slot width is w. The cross slot is centered at the null-voltage point of the simple triangular microstrip patch in the TM_{10} mode. It is then expected that due to the cross-slot perturbation, both the effective surface current paths of the two orthogonal resonant modes can be lengthened, which lowers their corresponding resonant frequencies. Thus, an antenna size reduction can be expected at a fixed frequency if the present compact CP design is used in place of the regular CP design in Fig. 1. The feed position at point C in the figure is for right-hand CP radiation, and point D is for left-hand CP radiation. And the distance of the feed position away from the cross-slot's center is given by d_p.

TABLE III
CP PERFORMANCE OF THE PROPOSED ANTENNA SHOWN IN FIG. 2; $d = 48$ mm, $\varepsilon_r = 4.4$, $h = 1.6$ mm, $w = 1$ mm, FEED AT POINT C. (a) ANTENNA 7: $\ell_S = 4.4$ mm, $l = 7.2$ mm, $d_p = 8.8$ mm. (b) ANTENNA 8: $\ell_S = 4.5$ mm, $l = 11$ mm, $d_p = 7.0$ mm. (c) ANTENNA 9: $\ell_S = 4.7$ mm, $l = 19.2$ mm, $d_p = 2.5$ mm

	ℓ (mm)	ℓ_S (mm)	d_p (mm)	Center frequency	CP bandwidth	Maximum received power
Antenna 7	7.2	4.4	8.8	1915 MHz	1.09%	-49.58 dBm
Antenna 8	11.0	4.5	7.0	1860 MHz	1.02%	-50.64 dBm
Antenna 9	19.2	4.7	2.5	1708 MHz	0.88%	-51.43 dBm

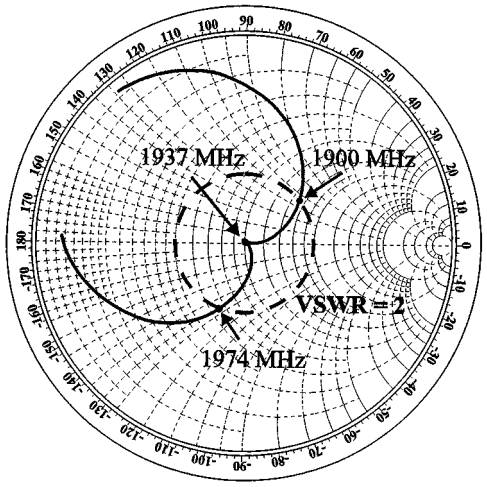

(a)

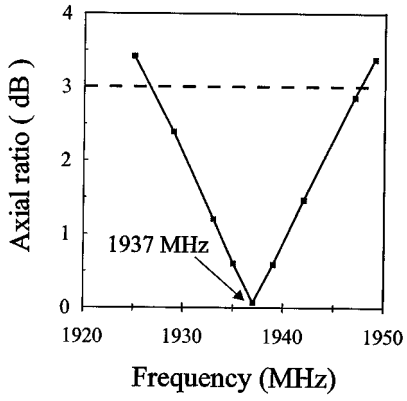

(b)

Fig. 3. Measured (a) input impedance and (b) axial ratio for antenna 2 with parameters in Table I.

III. RESULTS AND DISCUSSION

A. The Design with a Tuning Stub Loaded at the Triangle Tip

Three cases of different patch's side lengths (denoted as antennas 1, 2, and 3 here) are studied and the CP performance is given in Table I. Fig. 3 shows the measured input impedance and axial ratio for antenna 2. It can be seen that a dip in the impedance locus near their respective dominant resonant frequency is obtained, which indicates that two resonant modes are excited at very close frequencies and also suggests that

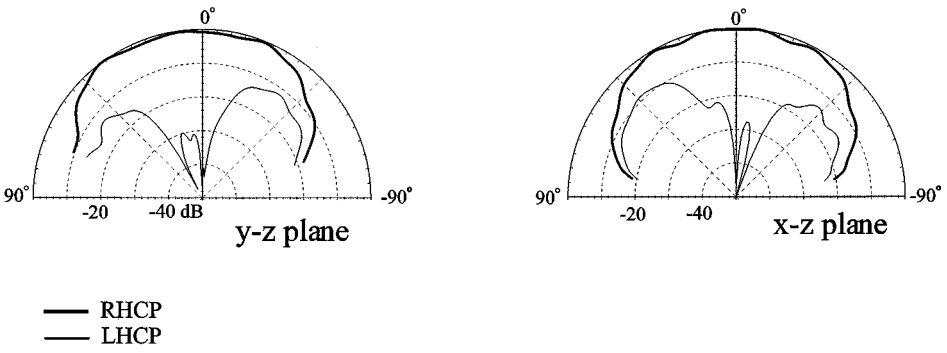

Fig. 4. Measured radiation patterns in two orthogonal planes for antenna 2 at 1937 MHz.

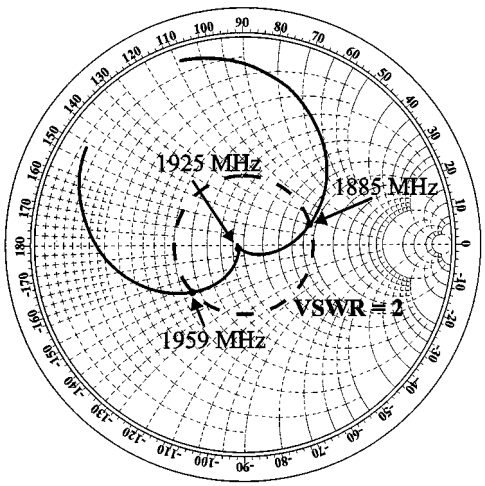

(a)

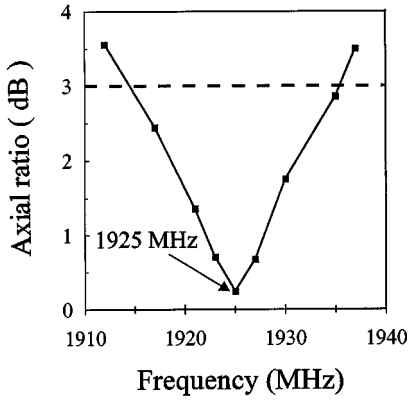

(b)

Fig. 5. Measured (a) input impedance and (b) axial ratio for antenna 5 with parameters in Table II.

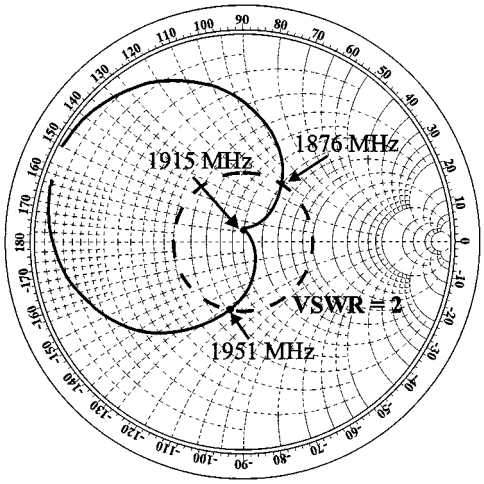

(a)

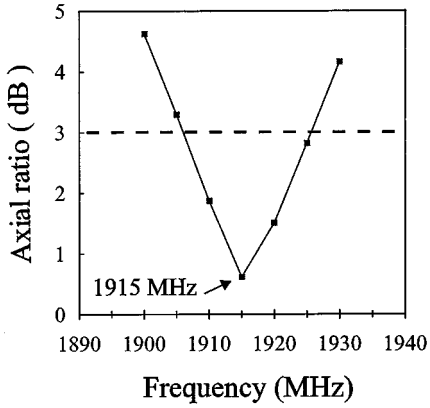

(b)

Fig. 6. Measured (a) input impedance and (b) axial ratio for antenna 7 with parameters in Table III.

the fundamental TM_{10} mode is split into two near-degenerate modes. Fig. 4 plots the measured radiation patterns for antenna 2 at the center frequency, the frequency with minimum axial ratio in the CP bandwidth. Good right-hand CP radiation is observed.

B. The Design with a Tuning Stub Loaded at the Bottom Edge

Three cases of antennas 4 to 6 are studied and the results are listed in Table II. The measured input impedance and axial ratio for antenna 5 is shown in Fig. 5. It is seen that when the tuning stub is at the triangle tip, the required tuning-stub length for CP radiation is much smaller than that in the design with the tuning stub at the bottom edge. This suggests that effect of the tuning-stub loading is more prominent at the triangle tip than at the bottom edge. Good right-hand CP radiation is also seen, and for brevity, measured radiation patterns are not shown here.

C. The Compact CP Design with a Tuning Stub and a Cross-Slot of Equal Slot Lengths

The compact CP design (Fig. 2) with three different cross-slot sizes (antennas 7, 8, and 9) is studied. The obtained CP performance is listed in Table III. Measured input impedance and axial ratio for antenna 7 are presented in Fig. 6. It is seen that the center CP frequency decreases with increasing cross-slot length. For antenna 9, the center frequency is lowered to 1708 MHz, which is about 88% times that (1937 MHz) of the regular-size CP design (antenna 2). This lowering in the center

frequency can correspond to an antenna size reduction of about 22% for using the present compact CP design in place of the CP design of Fig. 1(a). Also, good measured right-hand CP radiation patterns are obtained.

IV. Conclusion

Single-feed CP designs of equilateral-triangular microstrip antennas with a tuning stub have been experimentally investigated. Results show that it is most effective to achieve CP radiation by placing the tuning stub at the triangle tip. The application of the present CP design to a compact equilateral-triangular microstrip antenna with a cross-slot of equal slot lengths has also been studied. An antenna size reduction of about 22% as compared to the CP design of a regular triangular microstrip antenna at a fixed frequency can be obtained. For the regular and compact equilateral-triangular microstrip antennas studied, good CP radiation has also been obtained.

References

[1] Y. Suzuki, N. Miyano, and T. Chiba, "Circularly polarized radiation from singly fed equilateral-triangular microstrip antenna," *IEE Proc.-Microwave Antennas Propagat.*, vol. 134, pp. 194–198, Apr. 1987.

[2] J. H. Lu, C. L. Tang, and K. L. Wong, "Circular polarization design of a single-feed equilateral-triangular microstrip antenna," *Electron. Lett.*, vol. 34, pp. 319–321, Feb. 19, 1998.

[3] ——, "Single-feed slot-loaded equilateral-triangular microstrip antenna for circular polarization," *IEEE Trans. Antennas Propagat.*, vol. 47, pp. 1174–1178, Sept. 1999.

[4] C. L. Tang, J. H. Lu, and K. L. Wong, "Circularly polarized equilateral-triangular microstrip antenna with truncated tip," *Electron. Lett.*, vol. 34, pp. 1277–1278, June 25, 1998.

[5] K. L. Wong and Y. F. Lin, "Circularly polarized microstrip antenna with a tuning stub," *Electron. Lett.*, vol. 34, pp. 831–832, Apr. 30, 1998.

[6] J. H. Lu, H. C. Yu, and K. L. Wong, "Compact circular polarization design of equilateral-triangular microstrip antenna with spur lines," *Electron. Lett.*, vol. 34, pp. 1989–1990, Oct. 15, 1998.

[7] K. P. Yang, K. L. Wong, and J. H. Lu, "Compact circularly polarized triangular microstrip antenna with Y-shaped slot," *Microwave Opt. Technol. Lett.*, vol. 20, pp. 31–34, Jan. 5, 1999.